An Investigation of Implantable Capacitive Coupling Intra-body Power Transfer based on Full-band Loss Compensation

Cheng Han, *Student Member, IEEE*, Shan Yu, Zhiwei Zhang, and Jingna Mao, *Member, IEEE*

***Abstract*—Capacitive coupling intra-body power transfer (CC-IBPT) is a promising technique for powering implantable medical devices (IMDs) due to its flexible transmitter (TX) placement. However, several frequency-dependent capacitive impedances increase the path loss. Traditional methods have only compensated for partial path loss at the initially measured optimal frequency, which limits power transfer efficiency (PTE) enhancement. To address this issue, this article investigates the effect of full-band loss compensation (FBLC) on the transmission characteristics, both through theoretical analysis and implantation experiments to achieve maximum PTE at a system level. In the vector network analyzer-based simulation and measurement, FBLC achieves a higher path gain of 6.6 dB than conventional methods. Furthermore, we establish an implantable CC-IBPT prototype system to demonstrate the effects of FBLC on end-to-end power gain and PTE enhancement. The measured results indicate that with a 1 mm^2 square electrode implanted 4.6 cm deep in the pork tissue and positioned 15 cm away from the TX electrode, FBLC enhances PTE to 2.06%, an improvement of 3.55 times compared to 0.58% using conventional methods. This work demonstrates that FBLC achieves a higher PTE than traditional methods and validates the capability of CC-IBPT to achieve a relatively elevated PTE in long-distance wireless power supplies for IMDs.**

***Index Terms*—Capacitive coupled intra-body power transfer (CC-IBPT), full-band loss compensation (FBLC), implantable medical devices (IMDs).**

I. Introduction

IMPLANTABLE medical devices (IMDs) are widespread for patient treatment and recovery, such as neural stimulators [1], cardiac pacemakers [2], and retinal prosthesis [3]. However, the long-term power supply for IMDs remains a fundamental challenge. Compared to the battery-powered method, wireless power transfer (WPT) eliminates the need for frequent surgical operations and holds great potential to enable long-term implantation of miniaturized IMDs [4], [5]. The commonly used WPT techniques have unique features and advantages, such as superior power transfer efficiency (PTE) in near-field inductive coupling [6], [7], high delivered power in capacitive coupling [8], [9] and extended transfer distance in ultrasonic, mid-field, or far-field technologies [10], [11], [12]. However, strict device alignment and restricted transmission range will hinder the free activities of users.

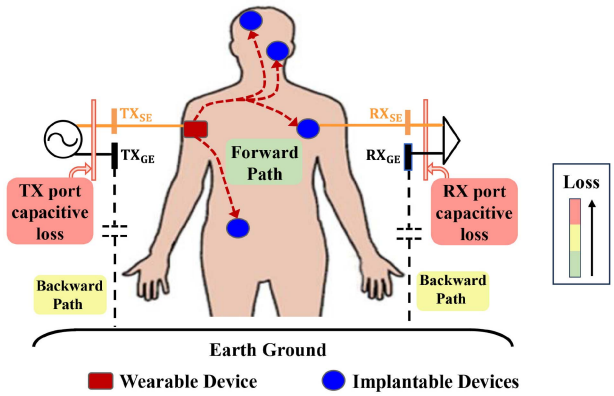

Fig. 1. Block diagram of the implantable CC-IBPT system.

Recently, the intra-body power transfer (IBPT) technology, which uses biological tissue as the medium has been investigated to power implantable bioelectronics. According to the fundamental theory, the IBPT technique can be categorized into two types, i.e., Galvanic coupled IBPT (GC-IBPT) and Capacitive coupled IBPT (CC-IBPT). In GC-IBPT, the power is delivered in the form of a loop current through two pairs of transmitter and receiver electrodes in contact with body tissue [13], [14]. However, the injection of a large current can be harmful to the human body, thus, the transmitter's location is limited to a close range of the implant in order to ensure enough power levels are received. In the case of CC-IBPT, there is no direct current loop to ensure human safety. The conceptual block diagram of CC-IBPT powering implantable devices is illustrated in Fig. 1. Only transmitter and receiver signal electrodes ($\mathrm{TX_{SE}}$ and $\mathrm{RX_{SE}}$) are in contact with body tissue, forming the conductive forward body

Manuscript received 9 October 2023; revised 31 December 2023 and 18 February 2024; accepted 5 March 2024. Date of publication 19 March 2024; date of current version 16 May 2024. This work was supported in part by the STI 2030—Major Projects 2021ZD0200402. Recommended for publication by Associate Editor A. Kuperman. *(Corresponding authors: Jingna Mao; Zhiwei Zhang.)*

Cheng Han is with the Institute of Automation, Chinese Academy of Sciences, Beijing 100190, China, and also with the School of Future Technology, University of Chinese Academy of Sciences, Beijing 100049, China (e-mail: hancheng2020@ia.ac.cn).

Jingna Mao is with the Institute of Automation, Chinese Academy of Sciences, Beijing 100190, China (e-mail: jingna.mao@ia.ac.cn).

Shan Yu and Zhiwei Zhang are with the Institute of Automation, Chinese Academy of Sciences, Beijing 100190, China, and also with the CAS Center for Excellence in Brain Science and Intelligence Technology, Shanghai 200031, China (e-mail: shan.yu@ia.ac.cn; zhiwei.zhang@ia.ac.cn).

Color versions of one or more figures in this article are available at https://doi.org/10.1109/TPEL.2024.3379118.

Digital Object Identifier 10.1109/TPEL.2024.3379118

path. The backward path is established via capacitive coupling between the earth ground and ground electrodes of TX and RX ($\mathrm{TX_{GE}}$ and $\mathrm{RX_{GE}}$), which are insulated from bio-tissue. In this way, the TX electrode can be placed anywhere on the body surface and the RX electrode is implanted within tissue to power IMDs like brain–machine interface. Consequently, CC-IBPT provides users greater freedom of movement without the need for device alignment, and the transmission range can be expanded to cover the entire body.

To further enhance the end-to-end PTE of the CC-IBPT system, path loss compensation is required. Path loss refers to the power consumed along the transmission path from the transmitter to the receiver front-end, which is composed of forward path transmission loss and dual port capacitive loss. Due to the higher conductivity of body tissue compared to air, the forward path transmission loss is relatively low. The dual port capacitive loss represents the port return loss of the two-port network between TX and RX electrode positions, which is primarily caused by large electrode-related and forward network ports' capacitive impedance. Several studies have been conducted to reduce the path loss of CC-IBPT. For instance, the proposed CC-IBPT system in [15] inserts a series inductor at the transmitter's output port to resonate with the backward coupling capacitance. In addition, the effect of capacitive impedance is reduced by increasing the transmitted voltage through impedance matching [16]. However, these works lack a comprehensive analysis of the entire path loss and only compensate for a portion of the dual port capacitive loss. Furthermore, the loss compensation is only performed at the originally measured optimal frequency, which cannot guarantee that the enhanced PTE reaches its maximum value. Since the dual port capacitive loss is frequency-dependent, it is possible to achieve a higher PTE by compensating for the loss at other frequency points. Therefore, existing loss compensation methods have limitations in further increasing the PTE of CC-IBPT.

In this article, we present an investigation of implantable CC-IBPT based on full-band loss compensation (FBLC) to achieve maximum end-to-end efficiency at a system level. Initially, we develop a lumped circuit model to analyze the factors that influence the total path loss and the impact of FBLC on the frequency characteristics of enhanced power gain. Then, we use a vector network analyzer (VNA) to measure CC-IBPT's transmission characteristics and confirm FBLC's enhancement effect on the path gain. In addition, a prototype system is built to assess the wireless power supply performance of implantable CC-IBPT in scenarios where the user can move freely, based on which the enhanced end-to-end PTE achieved by FBLC is validated. This can help identify the optimal operating frequency and then provide guidance for the practical system design and optimization to achieve high efficiency.

The rest of this article is organized as follows. In Section II, we conduct a theoretical analysis of the coupling mechanism and FBLC using the CC-IBPT model. Section III verifies the effectiveness of FBLC in improving path gain through a VNA. In Section IV, we present experimental results and comparisons of power gain in an implantable CC-IBPT prototype system with and without FBLC. Finally, Section V concludes this article.

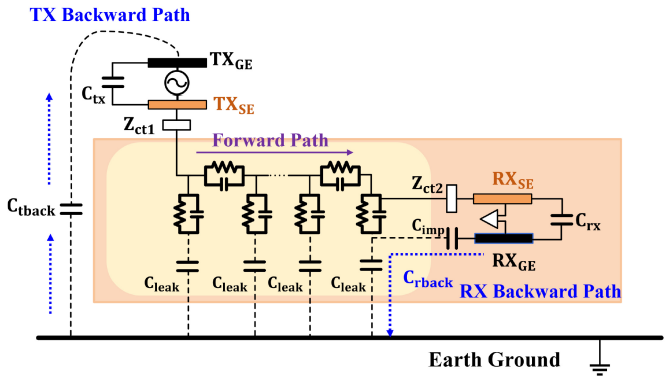

Fig. 2. Basic coupling mechanism scheme of CC-IBPT.

II. Theoretical Analysis

A. System Model of CC-IBPT

The basic coupling mechanism of CC-IBPT is depicted in Fig. 2. The conductive forward path can be perceived as a series of several π circuits, which encompasses the *RC* network of biological tissue and leakage capacitance C_{leak} between the body and the earth ground. The backward capacitive coupling exists at both the transmitter (TX) and receiver (RX) sides. As described in [17], the backward path capacitance C_{rback} coupled from the implanted RX to the ground plane is a series connection of body capacitance, which implies the leakage capacitance C_{leak} here, and the parasitic capacitance C_{imp} which is coupled between $\mathrm{RX_{GE}}$ and the surrounding body tissue. Moreover, the RX backward path impedance is dominated by C_{imp}. The backward path from the earth ground to the ground electrode of TX is established through their direct coupling capacitance, as denoted as C_{tback}. In addition, the usage of the electrode introduces additional capacitive impedances, including the self-coupling capacitance of TX and RX electrodes, which are represented by C_{tx} and C_{rx} respectively. The contact impedances represented by Z_{ct1} and Z_{ct2} are also considered, which signify the interface properties between the TX and RX signal electrode and the bio-tissue, respectively.

To facilitate path gain analysis, we built a circuit model of the implantable CC-IBPT system. First, the forward path is depicted as a two-port network to express body transmission properties. The conventional models for the body channel primarily consist of analytical models [18], finite element method (FEM) models [19], and circuit models [15], [17], [20], [21]. The equation-based analytical models make it hard to consider individual differences and adapt to the implantable CC-IBPT [18]. FEM models require long simulation times and repeated simulations for complex and diverse subjects [19]. As for circuit models, previous studies have simplified the forward path as a parallel circuit combination of *R* and *C*, treating the body as one node [15], [17]. However, this simplification is only suitable for low-frequency transmission scenarios (below 10 MHz with whole-body). The aforementioned models generally encounter limitations in their ability to adapt to diverse scenarios. The selected two-port network-based circuit model can incorporate

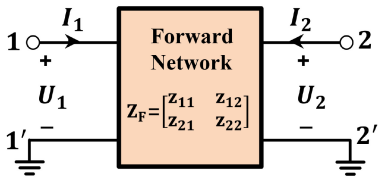

Fig. 3. Diagram of the forward network with Z-parameters.

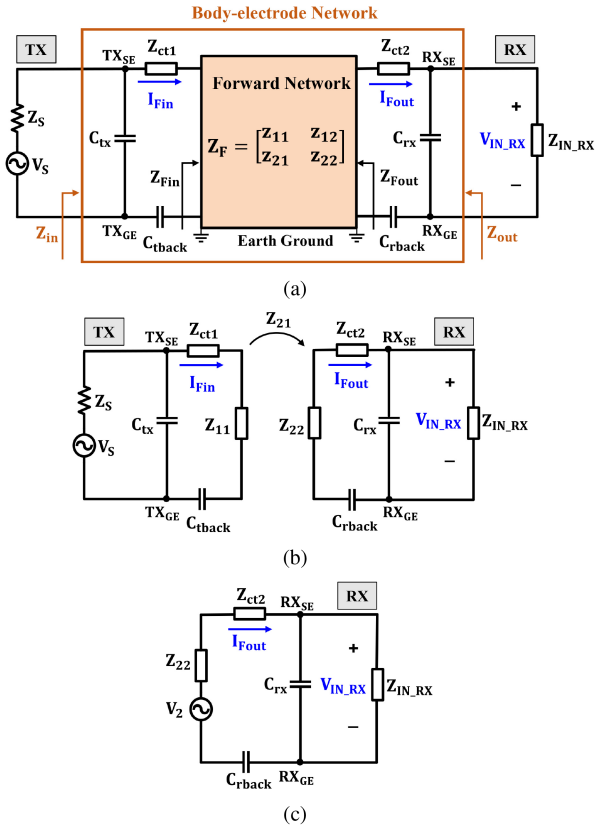

Fig. 4. Equivalent circuit of a general CC-IBPT system. (a) Established with a forward network. (b) Simplified with two parts. (c) Observed at the RX side.

various body channel properties including physiological characteristics, frequency-dependent dielectric properties, individual variations, etc., thus encapsulating the transmission characteristics comprehensively [20], [21]. The forward network diagram is shown in Fig. 3. The input (output) port 1-1' (2-2') is located between the tissue position of $\mathrm{TX_{SE}}$ ($\mathrm{RX_{SE}}$) and the earth ground. The symbols I_1 (I_2) and U_1 (U_2) represent the current and voltage at the 1-1' (2-2') port, respectively. An impedance matrix denoted as Z_F is employed to characterize the forward transmission properties, defined as follows:

$$\begin{bmatrix} U_1 \\ U_2 \end{bmatrix} = \begin{bmatrix} Z_{11} & Z_{12} \\ Z_{21} & Z_{22} \end{bmatrix} \begin{bmatrix} I_1 \\ I_2 \end{bmatrix}. \tag{1}$$

Based on the two-port network of the forward path, the overall equivalent circuit model of the implantable CC-IBPT system can be built, as presented in Fig. 4(a). The circuit includes a TX power source, an equivalent RX termination, a forward network, and the major parasitic impedances mentioned earlier. The other circuit components associated with the electrodes connect the forward network with the power source and RX termination. The symbols of I_{Fin} and I_{Fout} denote the actual current flowing into and out of the forward network, respectively. Z_{in}, Z_{Fin}, Z_{Fout}, and Z_{out} shown in Fig. 4(a) represent the input impedance of the remaining circuit as viewed from the indicated position. The circuit between the TX electrode and the RX electrode is referred to as a body-electrode network in this article for presentation purposes.

B. Path Gain Analysis

In a CC-IBPT system, the path gain is among the most significant performance factors. To provide a more intuitive analysis of the path gain (G_p) of the primary CC-IBPT system in Fig. 4(a), we derive a mathematical formula for G_p. In practical measurements, the TX port reflection coefficient S_{11} is minimally affected by the existence of the RX electrode (similarly for the RX port). Consequently, we divide the system circuit into two parts at the forward network position, as depicted in Fig. 4(b). The left circuit of the forward network can be analyzed independently, and its characteristics are then reflected into the right circuit through the Z_{21} parameter. In the left circuit, the current flowing into the forward network I_{Fin} is expressed using (2). Here, the input impedance of forward network Z_{Fin} approximately equals Z_{11}. In addition, for ease of validating path gain through experimentation, the source impedance Z_s and the input impedance of RX termination $Z_{\mathrm{IN\_RX}}$ are set to match the typical input impedance of the VNA, which is 50 Ω. As a result, Z_s is negligible when compared to Z_{in}, which allows for further simplification of I_{Fin} according to

$$\begin{aligned} I_{\mathrm{Fin}} &= \frac{Z_{\mathrm{in}}}{Z_{\mathrm{in}} + Z_s} \times \frac{V_s}{Z_{\mathrm{Fin}} + Z_{\mathrm{ct1}} + Z_{\mathrm{tback}}} \\ &\approx \frac{V_s}{Z_{11} + Z_{\mathrm{ct1}} + Z_{\mathrm{tback}}}. \end{aligned} \tag{2}$$

Upon analyzing the left circuit of the forward network, the complex model illustrated in Fig. 4(b) can be simplified to the configuration displayed in Fig. 4(c). V_2 denotes the open-circuit voltage at the output port of the forward network and can be expressed as the product of I_{Fin} and Z_{21}. The output impedance of the forward network Z_{Fout} is the series impedance, which is approximately equal to Z_{22}. The expression of RX voltage, $V_{\mathrm{IN\_RX}}$, is given in (3), where I_{Fout} represents the current flowing out of the forward network and Z_{rx} denotes the impedance of C_{rx}. Since $Z_{\mathrm{IN\_RX}}$ is set to 50 Ω, the parallel impedance of $Z_{\mathrm{IN\_RX}}$ and Z_{rx} is determined by $Z_{\mathrm{IN\_RX}}$ and is negligible when compared to the sum of other series impedances in the circuit. Thus, $V_{\mathrm{IN\_RX}}$ is further simplified. Subsequently, the path gain of the CC-IBPT's system can be derived in (4), by combining (2) and (3)

$$\begin{aligned} |V_{\mathrm{IN\_RX}}| &= |I_{\mathrm{Fout}} \times (Z_{\mathrm{rx}} // Z_{\mathrm{IN\_RX}})| \\ &= \left| \frac{V_2 \times Z_{\mathrm{rx}} // Z_{\mathrm{IN\_RX}}}{Z_{22} + Z_{\mathrm{ct2}} + Z_{\mathrm{rback}} + Z_{\mathrm{rx}} // Z_{\mathrm{IN\_RX}}} \right| \end{aligned}$$

$$\approx \left| \frac{I_{\text{Fin}} \times Z_{21} \times Z_{\text{IN\_RX}}}{Z_{22} + Z_{\text{ct2}} + Z_{\text{rback}}} \right| \tag{3}$$

$$G_p = \left(\left| \frac{2}{Z_{22} + Z_{\text{ct2}} + Z_{\text{rback}}} \right| \times \left| \frac{Z_{21} \times Z_{\text{IN\_RX}}}{Z_{11} + Z_{\text{ct1}} + Z_{\text{tback}}} \right| \right)^2. \tag{4}$$

The analysis of the path loss for the CC-IBPT system can be based on (4). The path loss is categorized into two types, i.e., forward path transmission loss and dual port capacitive loss. First, Z_{21} determines the forward path transmission loss, which is influenced by human body properties and transmission path. On the other hand, dual port capacitive loss refers to the power lost at both ports of the body-electrode network, which includes forward network port loss, contact loss, and backward path loss. The forward network port loss occurs due to the capacitive component presented in Z_{11} and Z_{22} that restrain active power transfer. In addition, contact loss occurs at the interface between the signal electrode and biological tissue. The electrode–tissue contact impedance (Z_{ct1} and Z_{ct2}) can be modeled as a parallel connection of a constant resistance and a capacitance [22]. It is mainly dominated by the electrode–body contact tightness and ensuring tight contact can reduce the loss to a minimum level. Furthermore, the remaining power loss is contributed by the backward coupling capacitance (Z_{tback} and Z_{rback}), which is affected by ground electrode size and human body shielding in the backward path. Although the specific value may vary under different experimental conditions, the components of G_p exhibit capacitive characteristics. Hence, the transmission frequency significantly impacts G_p, while its overall frequency trend remains consistent under various scenarios.

A quantitative analysis is performed to observe the frequency characteristics of G_p based on (4). It can be seen that the impedance Z_{21} results in a decline of G_p as the frequency increases. However, the product of the two capacitive impedances in the denominator decreases at a faster rate with frequency. $Z_{\text{IN\_RX}}$ remains a constant value of 50 Ω. Therefore, G_p exhibits an upward trend as the frequency increases, while the rate of increase falls until G_p reaches its peak at an optimal frequency f_p.

C. Full-Band Loss Compensation

The loss compensation method is studied to enhance the path gain of CC-IBPT. The above theoretical analysis indicates that the forward path transmission loss remains unchanged in a given scenario, while the port capacitive loss can be compensated at both TX and RX sides. On the TX side, increasing the current flowing into the forward network (I_{Fin}) can enhance V_2 and further improve the path gain. It can be observed from (2) that I_{Fin} is primarily limited by the capacitive components presented in Z_{11}, Z_{ct1}, and Z_{tback}. However, this limitation can be eliminated by adding an L-matching circuit between the transmitter and TX electrode, which ensures that I_{Fin} is solely influenced by the active resistance in Z_{ct1} and Z_{11}. Consequently, the TX port capacitive loss can be compensated. When the available active power is obtained at the input port of the body–electrode network, the flow-in current I_{Fin} reaches its maximum. Similarly, at the RX side, the maximum $V_{\text{IN\_RX}_{\text{max}}}$ can be achieved when all available power is transferred to the RX termination by conducting conjugate impedance matching between the RX electrode and RX termination. Unless specifically requested otherwise, FBLC is conducted at both the TX and RX sides to minimize the capacitive loss.

To achieve the highest path gain of CC-IBPT over the entire frequency band, the enhanced path gain is analyzed. By applying the maximum power transfer theorem, the maximum flow-in current $I_{\text{Fin}_{\text{max}}}$ is derived in (5). Since the self-capacitance of RX electrode C_{rx} in parallel with the RX termination consumes no active energy, the maximum power obtained at the RX electrode front-end is the same as that obtained by the RX termination. Thus, the maximum RX termination voltage $V_{\text{IN\_RX}_{\text{max}}}$ can be derived by considering the real part impedance of the body–electrode network as viewed from the RX electrode front-end, as shown in (6). These values are then utilized to obtain a mathematical expression for the maximum path gain, as shown in (7). Compared G_o with G_p, it can be observed that loss compensation has a significant impact on the properties of the enhanced path gain. First, the compensation for the loss caused by both electrode-associated and forward network ports' capacitive impedances results in the maximum available power transferred to the RX termination. Second, the frequency characteristics no longer emerge as an overall upward trend. Although all components in (7) decrease with frequency, the numerator and denominator obtain the same order, and Z_{21} includes an additional capacitive impedance. Thus, the enhanced path gain G_o reflects more properties of Z_{21} and the peak point f_o will shift to a lower frequency than f_p where Z_{21} begin to dominate the declining trend

$$I_{\text{Fin}_{\text{max}}} = \frac{V_s}{2\sqrt{Z_s \times Re(Z_{\text{ct1}} + Z_{11})}} \tag{5}$$

$$V_{\text{IN\_RX}_{\text{max}}} = \frac{I_{\text{Fin}_{\text{max}}} \times Z_{21}}{2} \times \sqrt{\frac{Z_{\text{IN\_RX}}}{Re(Z_{\text{ct2}} + Z_{22})}} \tag{6}$$

$$G_o = \left| \frac{Z_{21}^2}{4Re(Z_{\text{ct1}} + Z_{11}) \times Re(Z_{\text{ct2}} + Z_{22})} \right|. \tag{7}$$

D. End-to-end PTE Analysis

In a wireless power supply system, the end-to-end PTE plays a significant role in evaluating wireless performance. PTE is defined as the percentage ratio of the power received by the load (RX load power) P_L to the transmitted power (TX source power) P_S. As depicted in Fig. 5, a CC-IBPT RX (ac–dc converter) is commonly utilized to output dc power to the load R_L. The input impedance of the CC-IBPT RX corresponds to the RX termination impedance $Z_{\text{IN\_RX}}$ shown in Fig. 4(a). Since the maximum power received by RX with FBLC $P_{\text{IN\_RX}_{\text{max}}}$ is independent of $Z_{\text{IN\_RX}}$, the end-to-end PTE can be expressed by the products of maximum path gain G_o and the ac–dc conversion efficiency $\eta_{\text{ac–dc}}$, as derived in (8). The positive correlation between ac–dc conversion efficiency and the RX input power suggests that

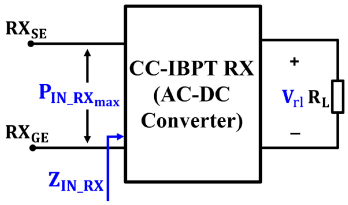

Fig. 5. Equivalent circuit at the receiver with FBLC.

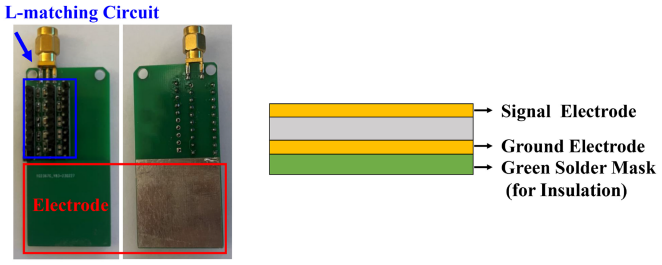

Fig. 6. (a) Electrode and L-matching circuit used in the experiment. (b) Diagram of the electrode.

the frequency characteristics trend of PTE largely keeps with the maximum path gain G_o, where the lower frequency band behaves better. Furthermore, to align the expression format with the path gain measured by VNA, PTE can also be represented in decibel (dB) form as the power gain G_{load} indicated in (9)

$$\begin{aligned}\text{PTE(FBLC)} &= \frac{P_L}{P_S} \times 100\% = G_o \times \eta_{\text{ac–dc}} \\ &= \left| \frac{Z_{21}^2}{4\text{Re}(Z_{\text{ct1}} + Z_{11}) \times \text{Re}(Z_{\text{ct2}} + Z_{22})} \right| \\ &\quad \times \frac{V_{\text{rl}}^2}{P_{\text{IN\_RX}_{\max}} \times R_L} \times 100\% \end{aligned} \tag{8}$$

$$G_{\text{load}} = 10 \lg \frac{P_L}{P_S}. \tag{9}$$

III. Verification of Path Gain Enhancement

A. VNA-Based Measurement Setup

In consideration of both convenient and effective experimental verification, a specialized electrode and L-matching circuit are implemented. Fig. 6 displays the copper electrodes of TX and RX, which are designed based on the electrode configuration proposed in [23]. They are implemented in a double-layer printed-circuit-board (PCB) fabricated with 1.6 mm thick FR-4 material. The bare copper layer serves as the signal electrode in contact with the bio-tissue, while the other copper layer coated by an insulating layer is utilized as the ground electrode. In addition, the L-matching circuit is integrated with the electrode. To perform tunable impedance matching throughout a wide frequency range and to accomplish the compensation experiment conveniently, several discrete inductors and capacitors controlled by the jumper cap are used to form the L-matching network. Although the size of the L-matching circuit used in our experiment is large, the backward path is not affected since the actual ground electrode size remains unchanged with the matching circuit being not designed with PCB Ground Plane. Therefore, the results of this verification experiment are still valid in the case of using a miniaturized L-matching circuit in the actual application.

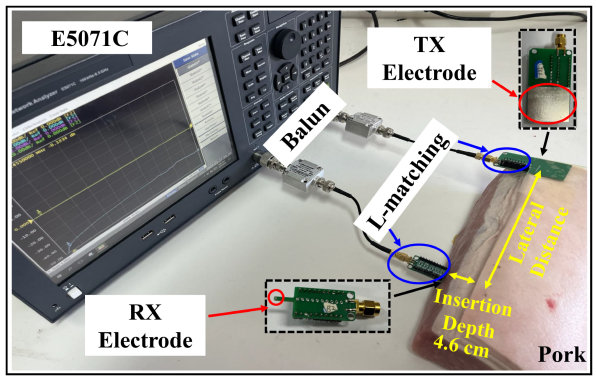

Fig. 7. Measurement setup for path gain.

To quickly obtain the path characteristics versus frequency, the S parameters of the body–electrode network are measured using a Keysight E5071C VNA, as displayed in Fig. 7. The experiment is carried out on a piece of pork with the dimension of 24 cm × 11 cm × 7.6 cm at room temperature. And the pork is positioned at a height of 70 cm from the earth ground. The pork is composed of three tissue layers including skin, fat, and muscle, with respective thicknesses of 0.1 cm, 2.5 cm, and 5 cm. A 3 cm × 3 cm TX electrode is affixed to the skin surface of the pork, while a square RX electrode with a length of 1 mm is implanted in the muscle layer at an insertion depth of 4.6 cm from the skin surface of the pork.

The lateral distance between the centers of TX and RX electrodes is maintained at 15 cm. To facilitate parameter adjustments for the L-matching circuit across multiple frequencies, the adjustable L-matching circuit is not implanted along with the RX electrode in this verification experiment. However, once the carrier frequency is determined in the actual application, a fixed miniaturized L-matching circuit can be implanted into bio-tissue along with the RX electrode. The VNA's frequency range is configured to span 1–60 MHz to encompass the transmission frequency adopted in previous related works [15], [16], [24]. In addition, the VNA's output power is set to 0 dBm. As illustrated in Section II-A, the backward path is formed by ground electrodes, so the isolation between the instrument ground and ground electrode has to be taken into account. To prevent a direct connection of the TX and RX ground electrodes through the common power line, a pair of baluns (FTB-1-1 from Mini-Circuits) is adopted to isolate them from the earth ground. The utilized balun operates within the frequency range of 0.2–500 MHz [25]. It has a smaller interwinding capacitance, which can reduce parasitic effects. The balun is directly fixed to the VNA to get rid of long cables. A total of 50 Ω-matched coaxial cable and SMA connector are employed to complete the connection. The cable length is kept as short as possible to prevent undesired attenuation. Besides, upon removal of the pork, the channel

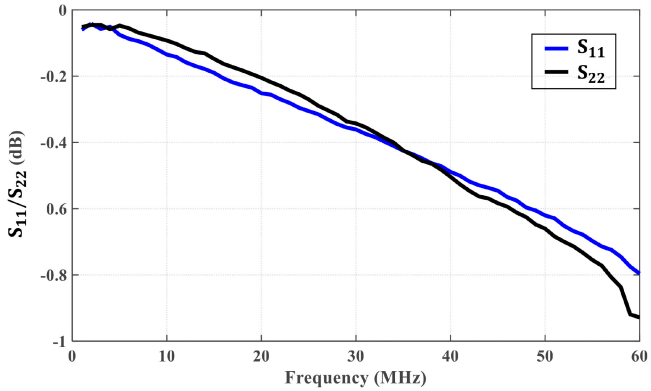

Fig. 8. Measured S_{11} and S_{22} without FBLC in the VNA measurement.

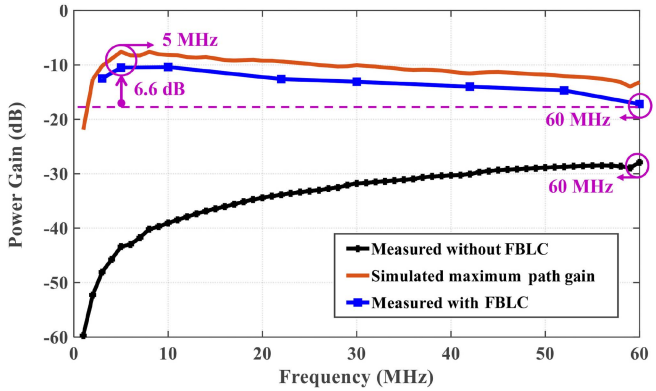

Fig. 9. Simulated and measured path gain of the body–electrode network.

gain contributed by the TX and RX cable/electrode coupling is measured to be less than −60 dB in the frequency band (1 MHz–60 MHz) and transmission range ($\geq$ 5 cm). It indicates the effect of TX and RX cable/electrode coupling on the power gain measurement of CC-IBPT is negligible. To eliminate the parasitic effects of baluns and cables, the calibration is performed carefully before each measurement.

FBLC can be achieved through theoretical simulation and practical experiments. The simulation setup is conducted in the Advanced Design System (ADS) software. The simulated frequency spans from 1 to 60 MHz, with a step size of 1 MHz. The S2P instance is filled with the measured S-parameter file that represents the path loss characteristics of CC-IBPT. Both the TX and RX ports are configured to the VNA's port impedance of 50 Ω. And the maximum path gain can be directly simulated. In practical experiments, it is complicated to implement loss compensation at every frequency point through the circuit. Thus, the L-matching circuit is only performed at several frequency points within the band to demonstrate the overall frequency trend of the minimum path loss. Since the TX and RX loss compensation are independent of each other, the TX (RX) L-matching parameters are adjusted to match the input (output) impedance of the body–electrode network to compensate for the TX (RX) port capacitive loss.

B. Path Loss Compensation Results

The measured characteristics of the body–electrode network are analyzed first. Fig. 8 illustrates the two-port power reflection characteristics of Fig. 4(a). The reflection coefficients of S_{11} and S_{22} behave badly, with both exceeding −1 dB. This indicates that the majority of available power is not transferred to the forward network and RX load. It also corresponds to the theoretical analysis that a large part of power is lost due to some capacitive coupling. Moreover, both S_{11} and S_{22} parameters undergo a linear decline with frequency. However, it can be observed from Fig. 9 that the rising rate of the measured power gain without FBLC versus frequency gradually slows down. To be specific, from 1 to 10 MHz, the power gain exhibits an increase of almost 20 dB, followed by a mere improvement of 12 dB from 10 to 60 MHz. Thus, it can be inferred that the power gain

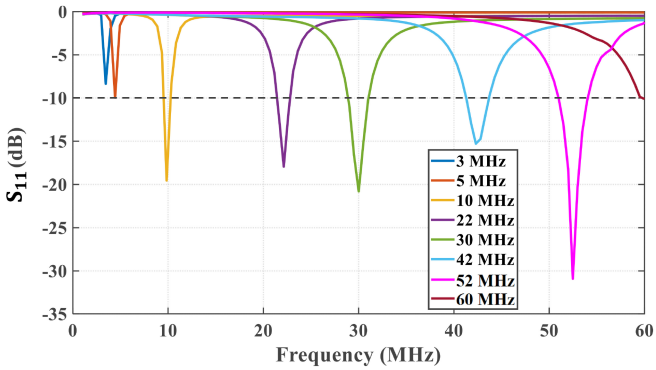

Fig. 10. Measured S_{11} with TX loss compensation.

in lower frequency bands may be more prominent after loss compensation.

Fig. 9 also exhibits the power gain versus frequency, both simulated and measured with FBLC. The simulated enhanced power gain shows a sharp rise trend in the low-frequency range, followed by a gradual decline as frequency increases. Furthermore, it can be observed that the power gain is increased by nearly 20 dB on average, and exceeds 35 dB at lower frequencies, which demonstrates the remarkable effect of loss compensation. In addition, the optimal frequency point shifts from 60 to 5 MHz. Compared to the simulated result, the fitted frequency characteristics of power gain obtained from the FBLC experiment are consistent in the variation trend and optimal frequency (5 MHz). As for the compensation effect, the measured power gain is almost 2–3 dB lower than the simulated value in the whole frequency band, which may be attributed to the inherent losses in inductors and capacitors of the L-matching circuit. Besides, as shown in Figs. 10 and 11, the S_{11} and S_{22} parameters compensated by L-matching circuits have been almost below −10 dB at the selected frequency point to ensure minimal ports' reflection losses.

Compared with conventional methods, which conduct loss compensation only at the originally measured optimal frequency, the proposed FBLC method for CC-IBPT can obtain a higher path gain. The maximum path gain through FBLC reaches −10.5 dB at 5 MHz, while the enhanced path gain at the

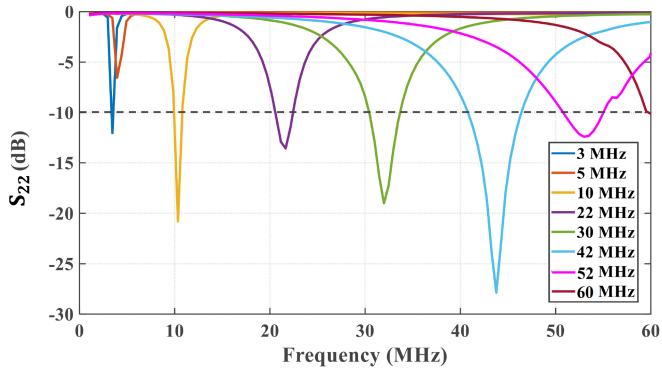

Fig. 11. Measured S_{22} with RX loss compensation.

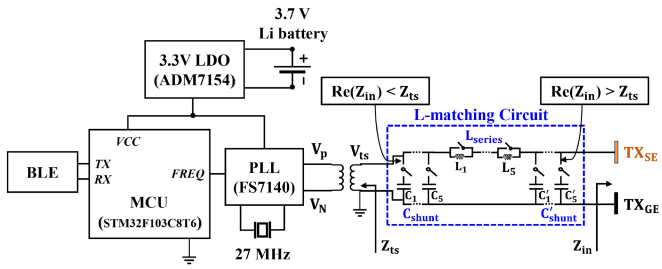

Fig. 12. Block diagram of the transmitter board.

originally measured optimal frequency of 60 MHz is −17.1 dB. Thus, the path gain is further enhanced by 6.6 dB through FBLC.

IV. Implantable CC-IBPT Prototype System

To investigate the end-to-end performance of CC-IBPT in powering implants, we establish a prototype system that incorporates the FBLC method. Furthermore, the proposed prototype system can mitigate the parasitic capacitance introduced by the balun in VNA measurements, ensuring a more accurate power gain.

A. Design of CC-IBPT

The CC-IBPT system includes a battery-powered transmitter and a rectifying receiver. The transmitter serves as the signal generator and is connected to an *LC* array circuit and the TX electrode. The block diagram of the TX board is depicted in Fig. 12. A low drop regulator (LDO) (ADM7154) supplies 3.3 V for other modules. A programmable phase-locked loop module (FS7140) is adopted to provide a differential clock signal. A balun converts the differential clock signals into a single-ended signal as the transmitting voltage V_{ts} with an open-circuit amplitude of 6.6 Vpp. The microcontroller (STM32F103C8T6) receives commands from the Bluetooth module and adjusts the transmission frequency. The operating frequency is set from 2 to 60 MHz at 2 MHz per step. The output impedance of the transmitter Z_{ts} is measured to be 60 Ω.

The receiver board is designed with the RX electrode, an L-matching circuit, and a voltage-doubler (VD) rectifier, as illustrated in Fig. 13. Although the full-wave rectifier obtains higher power conversion efficiency than the VD rectifier, the

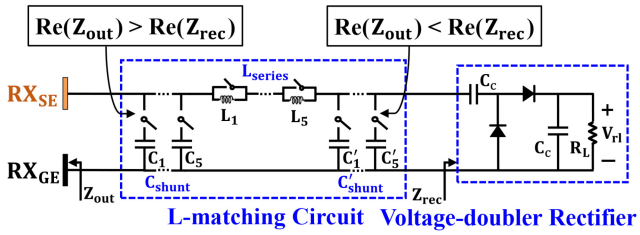

Fig. 13. Block diagram of the receiver board.

TABLE I
L-Matching Circuit Configuration

Freq.	TX		RX	
	L_{series}	C_{shunt} (C'_{shunt})	L_{series}	C_{shunt} (C'_{shunt})
2 MHz	51.8 μH	**30 pF**	125.7 μH	39 pF
4 MHz	39.4 μH	**1 pF**	55 μH	15 pF
8 MHz	6.99 μH	250 pF	18.98 μH	4 pF
20 MHz	1.82 μH	200 pF	5.52 μH	2 pF
30 MHz	0.85 μH	100 pF	2.46 μH	**15 pF**
40 MHz	0.40 μH	100 pF	1.64 μH	**10 pF**
50 MHz	0.30 μH	150 pF	1.04 μH	**10 pF**
60 MHz	0.08 μH	200 pF	0.82 μH	**8 pF**

Bold means C'_{shunt}; Unbold means C_{shunt}.

accurate input impedance measurement of the full-wave rectifier requires a true differential stimulus signal provided by a specific type and function of VNA [26]. However, the input impedance of the VD rectifier can be conveniently measured by a single-ended VNA. Thus, the VD rectifier is adopted in the prototype system to validate FBLC's effect on the enhancement of power gain. The rectifier circuit consists of two commercial diodes of SMS7630-079LF (SKYWORKS) and two capacitances C_c of 10 nF. The selected diode has a small forward voltage drop and a small junction capacitance of 0.3 pF, which can result in improved power conversion performance [27]. 1 kΩ resistor is chosen as the load R_L. The adjustable impedance matching circuit is inserted between the implanted RX electrode and the rectifier to optimize the received power. Moreover, the TX and RX electrode sizes remain the same as those in VNA measurements. The parameters of L-matching circuits for each measured frequency are summarized in Table I, which are adjusted through discrete inductors and capacitors soldered on the replaceable TX and RX boards.

B. Verification Setup

The verification setup is shown in Fig. 14, which is based on the designed CC-IBPT system. The experiment conditions remain consistent with those used in the experiment of measuring path properties. The recovered dc voltage at the RX load (V_{rl}) is measured by the multimeter.

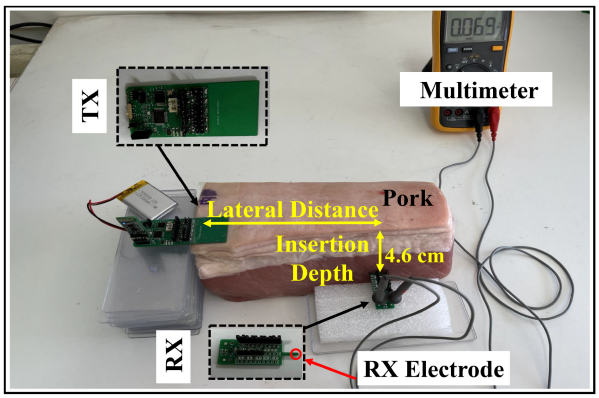

Fig. 14. Measurement setup for WPT performance.

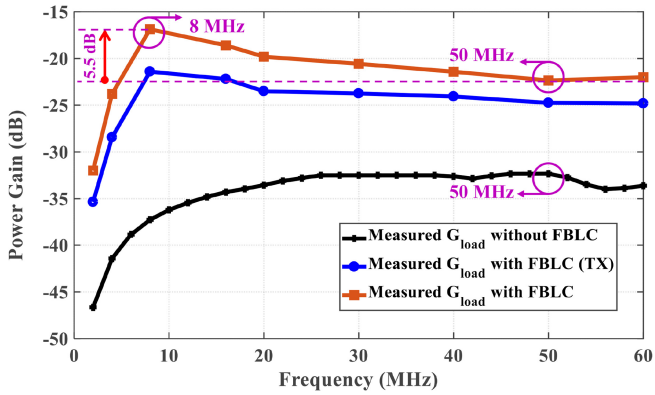

Fig. 15. Measured power gain versus frequency of the CC-IBPT prototype system.

To achieve FBLC during practical experiments, L-matching circuits' parameters are adjusted to match the output impedance of the transmitter (Z_{ts}) and the measured input impedance of the VD rectifier (Z_{rec}) with Z_{in} and Z_{out}, respectively. Due to the nonlinear impedance characteristics of the rectifier, we conducted a series of measurements on its input impedance with frequency by sweeping the power level output by VNA. Simultaneously, the recovered dc voltage is recorded. When the rectified load voltages measured in the CC-IBPT system and VNA are the same, the corresponding Z_{rec} can be determined. Since Z_{rec} varies with the rectifier's input power, FBLC is conducted sequentially to enhance the power gain. Specifically, the FBLC at the TX side (FBLC-TX) is first conducted. The RX L-matching circuit parameter is then adjusted based on Z_{rec} (FBLC-TX) to compensate for the RX impedance mismatch. Moreover, the measured results indicate that there is no significant variation in the rectifier's input impedance following the adoption of the RX L-matching circuit. Thus, the RX L-matching circuit parameters based on Z_{rec} (FBLC-TX) can ensure a well-matched impedance state at the RX port and achieve optimal performance.

C. Measured Results

The impact of FBLC on the frequency characteristics of end-to-end power gain for the CC-IBPT prototype system is studied. The measured results are shown in Fig. 15. The end-to-end power gain G_{load} of the CC-IBPT system is calculated according to

$$G_{\text{load}} = 10\lg\frac{P_L}{P_S} = 10\lg\frac{V_{\text{rl}}^2}{R_L}\times\frac{V_{\text{ts}}^2}{16Z_{\text{ts}}}. \tag{10}$$

The measured power gain of G_{load} without FBLC exhibits an initial rise followed by slight fluctuations. The maximum power gain is observed at 50 MHz. The implementation of FBLC-TX leads to a minimum increase of 9 dB in G_{load} and the dual-port FBLC further enhances RX load power by over 12 dB while causing significant changes in curve trends. When utilizing FBLC to reduce capacitive impedance's effect, the optimal frequency range shifts from 30 MHz–60 MHz to 8 MHz–20 MHz. In addition, the frequency response trend of G_{load} measured with FBLC is analogous to the simulated maximum power gain of the path curve illustrated in Fig. 9.

TABLE II
MEASURED POWER GAIN VERSUS LATERAL DISTANCE AT THE INSERTION DEPTH OF 4.6 CM

Lateral distance	5 cm	10 cm	15 cm
Without FBLC	-37.7 dB	-38.1 dB	-38.6 dB
With FBLC (TX)	-20.2 dB	-20.9 dB	-21.4 dB
With FBLC	-15.2 dB	-16.1 dB	-16.9 dB

Moreover, a maximum end-to-end power gain of −16.9 dB is achieved at the optimal frequency point of 8 MHz determined by FBLC, which is 5.5 dB higher than the enhanced power gain at the originally measured optimal frequency of 50 MHz. The enhanced PTE of 2.06% at 8 MHz is improved by 3.55 times more than that of 0.58% at 50 MHz. It can be inferred that FBLC significantly enhances RX load power to the maximum and shifts the optimal frequency towards lower frequencies.

To investigate the impact of transmission distance on the power gain of implantable CC-IBPT, we conducted measurements at various lateral distances and insertion depths while maintaining the optimal frequency determined by FBLC. First, the lateral distance is adjusted from 5 to 15 cm in 5 cm increments, while the RX insertion depth is fixed at 4.6 cm. The measured results are presented in Table II. It shows that the power gain decreases slightly when the lateral distance increases. This may be caused by the higher power loss in the forward network. Specifically, since the unchanged TX and RX electrodes are attached to the skin or implanted tightly in the same muscle tissue, the capacitive coupling and electrode-tissue interface conditions remain consistent. Consequently, all circuit components in the model depicted in Fig. 4(a) remain unchanged, except for the forward network. Since biological tissue has high conductivity and the forward network increases within the short range, the power gain is slightly reduced by about 1–2 dB. In addition, we explored the impact of insertion depth by implanting the RX electrode at depths of 3.6, 4.6, and 5.6 cm beneath the pork skin surface while maintaining a constant lateral distance of 15 cm. As shown in Table III, there is a slight decrease in the power

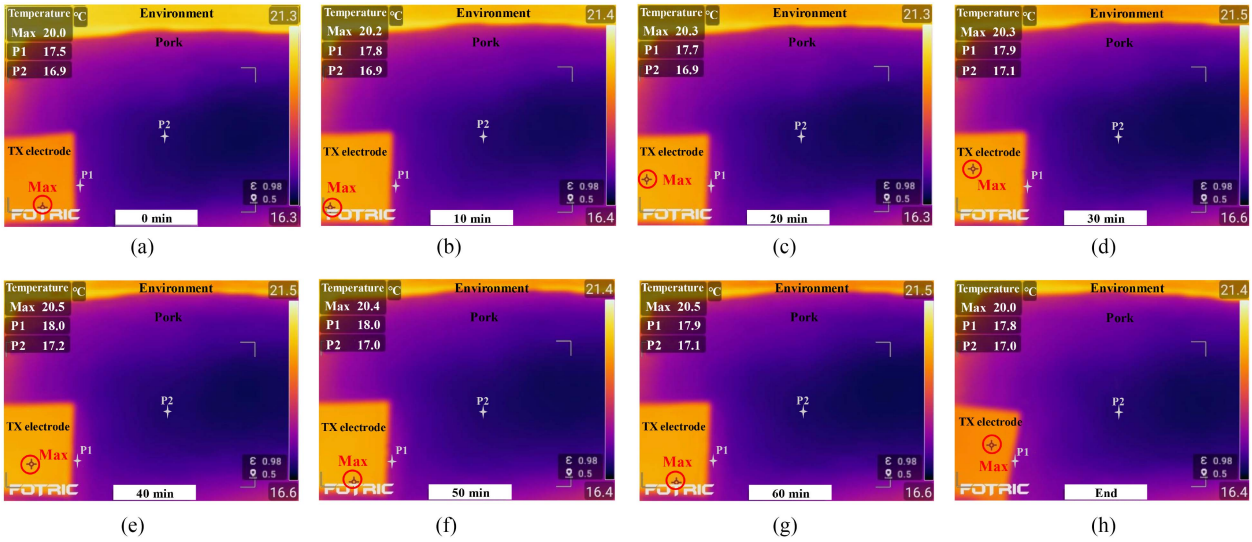

Fig. 16. Temperature measured by the thermal camera. (a) Before power transfer. (b)–(g) Images captured every 10 min during power transfer. (h) After power transfer ("Max" represents the highest temperature around TX electrode; "P1" and "P2" are random temperature observation points).

TABLE III
MEASURED POWER GAIN VERSUS INSERTION DEPTH AT THE LATERAL DISTANCE OF 15 CM

Insertion depth	3.6 cm	4.6 cm	5.6 cm
Without FBLC	-38.0 dB	-38.6 dB	-39.1 dB
With FBLC (TX)	-21.1 dB	-21.4 dB	-22.0 dB
With FBLC	-16.7 dB	-16.9 dB	-17.2 dB

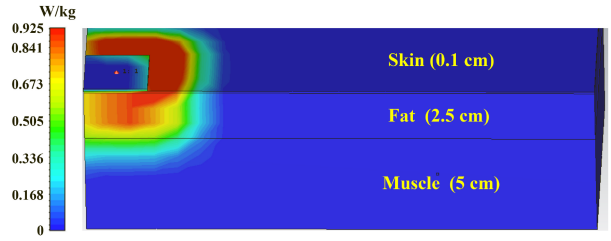

Fig. 17. Simulated SAR results.

gain as the insertion depth increases. Similarly, this is because the increased insertion depth causes higher power loss in the forward network. Due to the high conductivity of biological tissue and the centimeter-range increase in implantation depths, the decrease in power gain is less than 1.5 dB.

D. Safety Analysis

To ensure the safety of the human body, the temperature rise during power transfer and specific absorption rate (SAR) must be taken into consideration. Due to the highest transmitted power, the temperature around TX electrode is measured using a thermal camera (FOTRIC 321Q). Simultaneously, the PTE of the CC-IBPT system remains 2.06% at 8 MHz. Fig. 16 depicts the thermal images captured at 10-min intervals, as well as the stable period before and after power transfer. The measured results indicate that the maximum temperature rise within 60 min is 0.5 °C (from 20.0 °C at 0 min to 20.5 °C at 60 min), which is confirmed to be below the recommended upper limit for temperature rise (2 °C) [28]. Therefore, the temperature rise of CC-IBPT can ensure the human body's safety.

SAR simulation is conducted in the CST STUDIO SUITE software based on a tissue block with the same configuration as that used in the practical experiment above. The input power without reflection losses is adjusted to 45.38 mW, which corresponds to the situation of ideal impedance matching at the prototype system's TX side. The operation frequency is set at the measured optimal frequency of 8 MHz in the above experiment. The simulated result of the localized SAR over a 10 g tissue is shown in Fig. 17, where the maximum localized SAR value is 0.925 W/kg. This value falls below the partial-body exposed SAR safety limitation of 2 W/kg for persons in the unrestricted environment, as listed in Table IV [29]. Therefore, it can be concluded that the proposed CC-IBPT method for IMDs does not pose harm to human health.

E. Comparison With State-of-the-art

In order to comprehensively evaluate the performance of WPT, a figure of merit (FoM) is presented to balance key indicators. FoM takes three factors into account, which are PTE, transmission distance (d), and the implanted RX electrode/coil size ($\mathrm{RX_{size}}$), as shown in (11). The transmission distance d is calculated based on the lateral distance (L_d) and the insertion depth (D_d)

$$\mathrm{FoM} = \frac{d \times \mathrm{PTE}}{\sqrt{\mathrm{RX_{size}}}}$$
$$d = \sqrt{(L_d)^2 + (D_d)^2}. \tag{11}$$

TABLE IV
SAR LIMITS WITH FREQUENCIES FROM 100 KHZ TO 6 GHZ [29]

Exposure Condition	Persons in uncontrolled environments SAR (W/kg)	Persons in restricted environments SAR (W/kg)
Whole-body	0.08	0.4
Partial-body (head and torso)[a]	2	10
Partial-body (limbs and pinnae)[a]	4	20

[a] Peak spatial-averaged value over any 10 g of tissue in the shape of a cube.

TABLE V
PERFORMANCE SUMMARY AND COMPARISON

	TBioCAS'21 [30]	TAP'22 [31]	JSSC'20 [32]	JSSC'22 [33]	Nat.Biomed. Eng'20 [10]	AWP Letters'22 [11]	TPE'18 [13]	ASSCC'21^{+} [24]	**This work**
Method	Inductive	Magnetic Resonance Coupling	Capacitive	Magnetoelectric	Ultrasound	Mid-field	GC-IBPT	CC-IBPT	**CC-IBPT (FBLC)**
Medium	Porcine Head	Minced Pork	Beef Muscle	Porcine Tissue	Porcine Hindlimb Tissue	Porcine Muscle	Pork Tissue	Pork Tissue	**Pork Tissue**
Frequency	6.5/7.5 MHz	403 MHz	5 MHz	0.33 MHz	1.85 MHz	1.5 GHz	13.9 MHz	40.68 MHz	**8 MHz**
TX Power	202.8 mW†	79.48 mW†	NA	NA	19.4 mW	1 W	100 mW	26.4 mW	**45.38 mW**
Recovered Power	115 mW	33.7 mW	NA	NA	65 μW	5.6 mW	390 μW†	780 μW	**933 μW**
Transmission Distance	5 mm*	6 mm*	3 mm*	3.35 cm** (L_d: 1.5 cm, D_d: 3 cm)	5.504 cm** (L_d: 2.2 mm, D_d: 5.5 cm)	5.5 cm*	7.07 cm** (L_d: 5 cm, D_d: 5 cm)	14 cm	**15.69 cm** (L_d: 15 cm, D_d: 4.6 cm)**
RX Size$^{\divideontimes}$	30-mm diameter	25.5 mm × 25.5 mm	20 mm × 20 mm*	2 mm × 3 mm	0.52 mm^2	9 mm × 13 mm	0.3 mm × 1.3 mm	0.36 mm × 1.9 mm	**1 mm × 1 mm**
Power Transfer Efficiency	56.70%‡	42.40%	~50.4%	0.28%	0.33%	0.56%	0.39%	2.95%	**2.06%**
FoM	0.1066	0.0998	0.0535	0.0383	0.2519	0.0285	0.4415	4.9937	**3.2320**

$^{+}$ Measured with an earth-grounded signal generator.† Calculated based on PTE. * The insertion depth. (TX and RX are aligned in the transverse direction.) ** Calculated transmission distance based on: $d = \sqrt{(L_d)^2 + (D_d)^2}$, where L_d represents the lateral distance and D_d represents the insertion depth. $^{\divideontimes}$ the implanted electrode/coil size without receiver circuit.* Single copper substrate.‡ DC-to-DC efficiency.

The proposed CC-IBPT system's performance is compared with the state-of-the-art wireless powering techniques for IMDs in Table V. The PTE can reach 2.06% at a transmission distance of 15.69 cm when using a 1 mm^2-sized electrode implanted in the pork tissue. Although inductive, magnetic resonance and capacitive coupling based near field WPT methods in [30], [31], [32] can achieve higher PTE, our system achieves a transmission distance that is more than 25 times longer and an implanted electrode size that is at least 400 times smaller. In contrast, the other WPT methods listed in Table V perform relatively better in terms of transmission distance, which can be extended to a few centimeters. However, they exhibit relatively poor performance in PTE, at least 3.7 times lower than our system. The implanted CC-IBPT system proposed in [24] obtains a higher PTE due to the employment of an earth-grounded signal generator as the power source, which shortens the TX path and significantly reduces the power loss. However, our prototype system's portable and miniaturized transmitter design provides a more convenient and flexible application than that in [24]. Overall, the proposed CC-IBPT system exhibits superior FoM with flexible application among the recently reported works.

V. CONCLUSION

This article investigates the FBLC method to maximize the efficiency of the implantable CC-IBPT system. A circuit model of the implantable CC-IBPT is established to analyze the factors influencing transmission path losses and the necessity of FBLC in minimizing dual port capacitive loss in theory. Results from both simulations and experimental measurements using a VNA confirm the superior effect of FBLC in achieving a higher path gain, with a significant improvement of 6.6 dB compared to the traditional method which compensates for loss at the initially measured frequency. Furthermore, the FBLC causes the optimal frequency to shift to a lower frequency point and reflects more frequency characteristics of the forward transmission path. To demonstrate the WPT performance with FBLC, a battery-powered CC-IBPT prototype system is developed. The

TABLE VI
NOMINAL VALUE RANGES FOR EACH COMPONENT IN FIG. 2

Component	Value	Comments
C_{tx}	22.5 pF	Calculated based on the capacitance formula of parallel plate capacitor
C_{rx}	0.026 pF	ditto
Z_{ct1}	hundreds of pF // hundreds of ohms	be referenced to [22]
Z_{ct2}	hundreds of pF// hundreds of ohms	ditto
C_{tback}	1.5 pF	Calculated based on [34]
C_{rback}	$<$1 pF	be referenced to [17]
C_{leak}	$<$1 pF	Depends on the segment number

measured results prove that the highest PTE can reach 2.06% at a new optimal frequency for a 1 mm^2 RX electrode implanted 4.6 cm deep in pork tissue, with a lateral distance of 15 cm. Moreover, FBLC enhances the end-to-end power gain by an additional 5.5 dB than traditional compensation. After determining the optimal frequency using the FBLC method, the adjustable L-matching circuits can be replaced by fixed compensation circuits of smaller sizes. Furthermore, the transmitter will be affixed to the user's body surface for power transmission, while the prototype receiver will be optimized and integrated with a power management circuit and other medical device modules on a chip to achieve miniaturized implantation applications.

Based on the FBLC method, this study verifies that the implanted CC-IBPT technique can achieve a relatively high PTE, while simultaneously maintaining a long transmission distance, user convenience, small electrode size, etc. Therefore, CC-IBPT is expected to be one of the best candidates for powering IMDs in diverse application scenarios, such as wirelessly powering a brain-machine interface chip implanted in freely behaving animals.

APPENDIX

The nominal value ranges for each component in Fig. 2 are listed in Table VI, which are determined based on the experimental setup and relevant prior research. To be specific, both TX and RX electrodes can be considered as parallel plate capacitors, with self-coupling capacitances C_{tx} and C_{rx} calculated using the formula $C = \epsilon S/d$, where ϵ represents the permittivity, S denotes the electrode area, and d is the distance between the signal and ground electrodes. According to the investigation in [22], the contact impedances Z_{ct1} and Z_{ct2} can be specified within the ranges of hundreds of pF // hundreds of ohms. The TX backward capacitance C_{tback} can be calculated as 1.5 pF using the formula presented in [34]. Besides, the RX backward capacitance C_{rback} which is dominated by the parasitic capacitance C_{imp} is cited as < 1 pF [17]. In addition, the value of C_{leak} mainly depends on the modeling segments of the body tissue. To make the model error converge to the minimum with increasing segment numbers, C_{leak} is set to be < 1 pF. The value range has also been utilized in numerous simulation studies [21], [35].

REFERENCES

[1] J. C. Chen et al., "A wireless millimetric magnetoelectric implant for the endovascular stimulation of peripheral nerves," *Nature Biomed. Eng.*, vol. 6, no. 6, pp. 706–716, Jun. 2022.

[2] C. Xiao, D. Cheng, and K. Wei, "An LCC-C compensated wireless charging system for implantable cardiac pacemakers: Theory, experiment, and safety evaluation," *IEEE Trans. Power Electron.*, vol. 33, no. 6, pp. 4894–4905, Jun. 2018.

[3] I. A. Mashhadi, M. Pahlevani, S. Hor, H. Pahlevani, and E. Adib, "A new wireless power-transfer circuit for retinal prosthesis," *IEEE Trans. Power Electron.*, vol. 34, no. 7, pp. 6425–6439, Jul. 2019.

[4] S. Roy, A. N. M. W. Azad, S. Baidya, M. K. Alam, and F. Khan, "Powering solutions for biomedical sensors and implants inside the human body: A comprehensive review on energy harvesting units, energy storage, and wireless power transfer techniques," *IEEE Trans. Power Electron.*, vol. 37, no. 10, pp. 12237–12263, Oct. 2022.

[5] S. Roy, A. N. M. W. Azad, S. Baidya, and F. Khan, "A comprehensive review on rectifiers, linear regulators, and switched-mode power processing techniques for biomedical sensors and implants utilizing in-body energy harvesting and external power delivery," *IEEE Trans. Power Electron.*, vol. 36, no. 11, pp. 12721–12745, Nov. 2021.

[6] O. Knecht and J. W. Kolar, "Performance evaluation of series- compensated IPT systems for transcutaneous energy transfer," *IEEE Trans. Power Electron.*, vol. 34, no. 1, pp. 438–451, Jan. 2019.

[7] J. Gao et al., "Design and optimization of a novel double-layer helmholtz coil for wirelessly powering a capsule robot," *IEEE Trans. Power Electron.*, vol. 39, no. 1, pp. 1826–1839, Jan. 2024.

[8] R. Sedehi et al., "A wireless power method for deeply implanted biomedical devices via capacitively coupled conductive power transfer," *IEEE Trans. Power Electron.*, vol. 36, no. 2, pp. 1870–1882, Feb. 2021.

[9] Z. Liu, Y. Su, H. Hu, Z. Deng, and R. Deng, "Research on transfer mechanism and power improvement technology of the SCC-WPT system," *IEEE Trans. Power Electron.*, vol. 38, no. 1, pp. 1324–1335, Jan. 2023.

[10] D. K. Piech et al., "A wireless millimetre-scale implantable neural stimulator with ultrasonically powered bidirectional communication," *Nature Biomed. Eng.*, vol. 4, pp. 207–222, Feb. 2020.

[11] N. Nguyen, N. Ha-Van, and C. Seo, "Midfield wireless power transfer for deep-tissue biomedical implants," *IEEE Antennas Wireless Propag. Lett.*, vol. 19, no. 12, pp. 2270–2274, Dec. 2020.

[12] C. Liu, Y.-X. Guo, H. Sun, and S. Xiao, "Design and safety considerations of an implantable rectenna for far-field wireless power transfer," *IEEE Trans. Antennas Propag.*, vol. 62, no. 11, pp. 5798–5806, Nov. 2014.

[13] P. Chen, H. Yang, R. Luo, and B. Zhao, "A tissue-channel transcutaneous power transfer technique for implantable devices," *IEEE Trans. Power Electron.*, vol. 33, no. 11, pp. 9753–9761, Nov. 2018.

[14] B. Chatterjee et al., "A 1.15 μW 5.54 mm^3 implant with a bidirectional neural sensor and stimulator SoC utilizing Bi-phasic quasi-static brain communication achieving 6 Kbps-10 Mbps uplink with compressive sensing and RO-PUF based collision avoidance," in *Proc. Symp. Very Large Scale Integration Circuits*, 2021, pp. 1–2.

[15] H. Cho, J.-H. Suh, C. Kim, S. Ha, and M. Je, "An intra-body power transfer system with -mW power delivered to the load and 3.3-V DC output at 160-cm of on-body distance," *IEEE Trans. Biomed. Circuits Syst.*, vol. 16, no. 5, pp. 852–866, Oct. 2022.

[16] J. Li, Y. Dong, J. H. Park, L. Lin, T. Tang, and J. Yoo, "Body-area powering with human body-coupled power transmission and energy harvesting ICs," *IEEE Trans. Biomed. Circuits Syst.*, vol. 14, no. 6, pp. 1263–1273, Dec. 2020.

[17] C. Lee et al., "A miniaturized wireless neural implant with body-coupled power delivery and data transmission," *IEEE J. Solid-State Circuits*, vol. 57, no. 11, pp. 3212–3227, Nov. 2022.

[18] J. Bae, H. Cho, K. Song, H. Lee, and H.-J. Yoo, "The signal transmission mechanism on the surface of human body for body channel communication," *IEEE Trans. Microw. Theory Techn.*, vol. 60, no. 3, pp. 582–593, Mar. 2012.
[19] A. Datta et al., "Sub-GHz in-body to out-of-body communication channel modeling for ruminant animals for smart animal agriculture," *IEEE Trans. Biomed. Eng.*, vol. 70, no. 4, pp. 1219–1230, Apr. 2023.
[20] H. Wang et al., "Cascaded network body channel model for intrabody communication," *IEEE J. Biomed. Health Informat.*, vol. 20, no. 4, pp. 1044–1052, Jul. 2016.
[21] J. Mao, H. Yang, Y. Lian, and B. Zhao, "A five-tissue-layer human body communication circuit model tunable to individual characteristics," *IEEE Trans. Biomed. Circuits Syst.*, vol. 12, no. 2, pp. 303–312, Apr. 2018.
[22] S. Maity, M. He, M. Nath, D. Das, B. Chatterjee, and S. Sen, "Biophysical modeling, characterization, and optimization of electroquasistatic human body communication," *IEEE Trans. Biomed. Eng.*, vol. 66, no. 6, pp. 1791–1802, Jun. 2019.
[23] M. Li et al., "Comparable investigation of characteristics for implant intra-body communication based on galvanic and capacitive coupling," *IEEE Trans. Biomed. Circuits Syst.*, vol. 13, no. 6, pp. 1747–1758, Dec. 2019.
[24] B. Kim, B. Yuk, and J. Bae, "A wirelessly-powered 10 Mbps 46-pJ/b body channel communication system with 45% PCE multi-stage and multi-source rectifier for neural interface applications," in *Proc. IEEE Asian Solid-State Circuits Conf.*, 2021, pp. 1–3.
[25] "FTB-1-1." Accessed: Aug. 2023. [Online]. Available: https://www.minicircuits.com
[26] K. Kotani, A. Sasaki, and T. Ito, "High-efficiency differential-drive CMOS rectifier for UHF RFIDs," *IEEE J. Solid-State Circuits*, vol. 44, no. 11, pp. 3011–3018, Nov. 2009.
[27] "SMS7630, ShottkyDiode, SKYWORKSCompany," 2015. [Online]. Available: http://www.skyworksinc.com/Product/512/SMS7630-061
[28] International Commission on Non-Ionizing Radiation Protection, "Guidelines for limiting exposure to time-varying electric, magnetic, and electromagnetic fields (up to 300 GHz)," *Health Phys.*, vol. 74, no. 4, pp. 494–522, 1998.
[29] *IEEE Standard for Safety Levels with Respect to Human Exposure to Electric, Magnetic, and Electromagnetic Fields, 0 Hz to 300 GHz*, IEEE Std C95.1-2019 (Revision of IEEE Standard C95.1-2005/ Incorporates IEEE Standard C95.1-2019/Cor 1-2019), 2019, pp. 1–312.
[30] Y. Park et al., "A wireless power and data transfer IC for neural prostheses using a single inductive link with frequency-splitting characteristic," *IEEE Trans. Biomed. Circuits Syst.*, vol. 15, no. 6, pp. 1306–1319, Dec. 2021.
[31] J. Wang et al., "A 403 MHz wireless power transfer system with tuned split-ring loops for implantable medical devices," *IEEE Trans. Antennas Propag.*, vol. 70, no. 2, pp. 1355–1366, Feb. 2022.
[32] R. Erfani, F. Marefat, S. Nag, and P. Mohseni, "A 1–10-MHz frequency aware CMOS active rectifier with dual-loop adaptive delay compensation and -mW output power for capacitively powered biomedical implants," *IEEE J. Solid-State Circuits*, vol. 55, no. 3, pp. 756–766, Mar. 2020.
[33] Z. Yu et al., "Magnetoelectric bio-implants powered and programmed by a single transmitter for coordinated multisite stimulation," *IEEE J. Solid-State Circuits*, vol. 57, no. 3, pp. 818–830, Mar. 2022.
[34] J. Mao, H. Yang, and B. Zhao, "An investigation on ground electrodes of capacitive coupling human body communication," *IEEE Trans. Biomed. Circuits Syst.*, vol. 11, no. 4, pp. 910–919, Aug. 2017.
[35] M. D. Pereira, G. A. Alvarez-Botero, and F. Rangel de Sousa, "Characterization and modeling of the capacitive HBC channel," *IEEE Trans. Instrum. Meas.*, vol. 64, no. 10, pp. 2626–2635, Oct. 2015.

Cheng Han (Student Member, IEEE) received the B.E. degree in automation from the School of Control Science and Engineering, Shandong University, Jinan, China, in 2020. She is currently working toward the the Ph.D. degree in pattern recognition and intelligent system with the Institute of Automation, Chinese Academy of Sciences, Beijing, China, also with School of Future Technology, University of Chinese Academy of Science, Beijing, China.

Her current study interests include wireless power transfer, and brain–machine interface.

Shan Yu received the B.S. and Ph.D. degrees in biology from the University of Science and Technology of China, Hefei, China, in 2000 and 2005, respectively.

From 2005 to 2014, he conducted Postdoctoral Research with the Max-Planck Institute of Brain Research, Germany (2005–2008), and the National Institute of Mental Health, USA (2008– 2014). After that, he joined the Institute of Automation, Chinese Academy of Sciences (CASIA). He is currently a Professor with CASIA. He has authored or coauthored more than 30 peer-reviewed articles in neuroscience and other interdisciplinary fields at leading journals, such as the Nature Machine Intelligence, the Journal of Neuroscience, and eLife. His current research interests include neuronal information processing, brain-inspired computing, and brain–machine interface.

Zhiwei Zhang received the Ph.D. degree in computer application technology from National Engineering & Technology Research Center for ASIC Design, the Institute of Automation, Chinese Academy of Sciences, Beijing, China, in 2008.

He is currently a Professor with the Institute of Automation, Chinese Academy of Sciences, Beijing, China. His current research interests include brain computer interface chip, digital signal processing chip, microprocessor architecture, and high-performance implementation technology of microprocessor.

Jingna Mao (Member, IEEE) received the B.E. degree in electronic science and technology from the Department of Electronic Engineering, Beijing Jiao Tong University, Beijing, China, in 2013 and the Ph.D. degree in electronic science and technology from the Department of Electronic Engineering, Tsinghua University, Beijing, China, in 2018.

She is currently an Associate Professor with the Institute of Automation, Chinese Academy of Science, Beijing, China. She has authored or co-authored around 30 technical papers. Her current research interests include brain–machine interface, body channel communication, wireless power transfer, and biometric identification.